Topological dissipative Kerr soliton combs in a valley photonic crystal resonator

Zhen Jiang,[1,2] Lefeng Zhou,[1] Wei Li,[3] Yudong Li [ORCID],[3] Liangsen Feng,[3] Tengfei Wu,[3]
Chun Jiang,[1,*] and Guangqiang He [ORCID][1,2,†]

[1]*State Key Laboratory of Advanced Optical Communication Systems and Networks, Department of Electronic Engineering,*
Shanghai Jiao Tong University, Shanghai 200240, People's Republic of China
[2]*SJTU Pinghu Institute of Intelligent Optoelectronics, Department of Electronic Engineering,*
Shanghai Jiao Tong University, Shanghai 200240, People's Republic of China
[3]*Science and Technology on Metrology and Calibration Laboratory, Changcheng Institute of Metrology & Measurement,*
Aviation Industry Corporation of China, Beijing 100095, People's Republic of China

Topological phases have become an enabling role in exploiting new applications of nonlinear optics in recent years. Here we theoretically propose a valley photonic crystal resonator emulating topologically protected dissipative Kerr soliton combs. It is shown that topological resonator modes can be observed in the resonator. Moreover, we also simulate the dynamic evolution of the topological resonator with the injection of a continuous-wave pump laser. We find that the topological optical frequency combs evolve from Turing rolls to chaotic states, and eventually into single soliton states. More importantly, such dissipative Kerr soliton combs generated in the resonator are inborn topologically protected, showing robustness against sharp bends and structural disorders. Our design supporting topologically protected dissipative Kerr soliton combs could be implemented experimentally in on-chip nanofabricated photonic devices.

I. INTRODUCTION

Optical frequency combs have been undergoing revolutionized development in integrated photonic resonators. For coherent optical frequency combs in microresonators, there exist stationary temporal solutions, so-called dissipative Kerr solitons (DKSs). Such DKSs are attributed to the double balance between the microresonator Kerr effect and dispersion management, as well as losses and parametric gain [1]. This specific phenomenon of optical frequency combs has exploited numerous concepts, such as the Stokes soliton [2], breathing solitons [3], and soliton crystals [4]. Primitively, bulk crystalline and microdisks [5–7] are proven to be an appropriate breeding ground for DKS combs. Furthermore, the soliton combs are expanded to on-chip photonic devices including Si_3N_4 [8–10], $LiNbO_3$ [11,12], and AlGaAs [13].

At the same time, topological phases of matter bring robustness to photonic devices. Advances in topological phases also excite sparks in nonlinear photonic systems. It has been experimentally proposed that the topological transport of second or third-harmonic waves can be conducted in chip-scale devices [14,15]. Furthermore, such systems exhibit the topological protection of four-wave mixing processes [16], topological optical frequency combs, and temporal DKSs [17,18]. Topological nonlinear optics also gives inspiration for implementing topological protection of complex nonlinear processes, including topological exciton polaritons [19,20]

and gap solitons [21,22]. The topological platforms are also applied to build topological protection of quantum states, such as topological quantum sources [23], entangled states [24–26], and quantum interference [27]. Recent researches have proposed a topological phase, namely the quantum valley Hall (QVH) effect [28–32], to implement valley kink states along the topological interface. Topological DKSs in coupled resonator arrays emulating the Su-Schrieffer-Heeger (SSH) model have been proposed [17,33]. However, the underlying aspects of topological DKSs in the QVH system with super-compact chip scaling have not been investigated yet. On the one hand, the complex resonator arrays restrict the chip scaling and lead to inconvenience for optical modulation. On the other hand, the nonlinear dynamic evolution of the Kerr solitons in such complex arrays of coupled rings leads to the complexity of the simulated model.

Here we theoretically investigate the generation and topological transport of DKS combs in a valley photonic crystal (VPC) slab. We confirm the existence of topologically protected kink states at the resonator modes in a whisper-gallery resonator. The nonlinear dynamic evolution of the topological resonator with an excited continuous-wave (CW) pump laser is numerically simulated. The result reveals that with the detuning of the pump laser, the optical frequency combs generated in the resonator can evolve into single soliton combs eventually. More importantly, these DKSs generated in the VPC resonator are topologically protected and show robustness against sharp bends and structural imperfections. Our design may give a new spark to the chip-scale operation of topological optical frequency combs.

_____
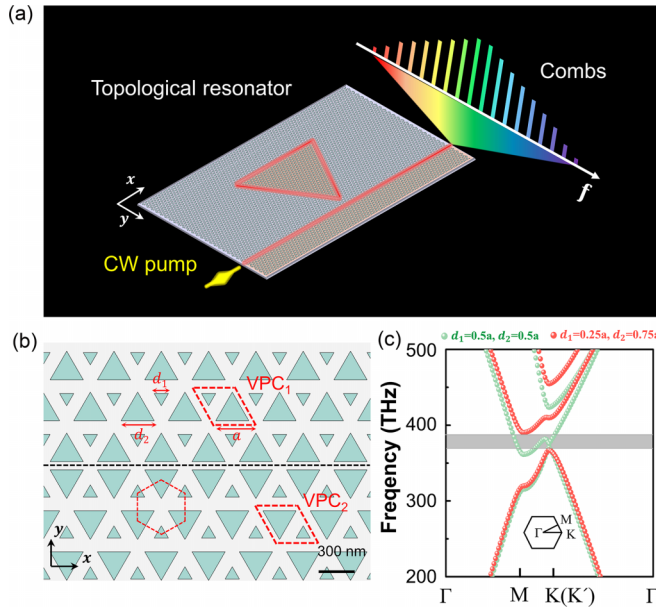
*cjiang@sjtu.edu.cn
†gqhe@sjtu.edu.cn

FIG. 1. (a) A scheme of VPC topological resonators enforcing the DKS combs. (b) 2D close-up image of VPCs with lattice constant $a = 300$ nm. (c) Calculated band structures of different VPCs, where the undeformed unit cells ($d_1 = d_2 = 0.5a$) and deformed unit cells ($d_1 = 0.25a$, $d_2 = 0.75a$) are denoted by green and red dots, respectively. The Γ, K, and M denote the high-symmetry points in the first Brillouin zone.

II. TOPOLOGICAL RESONATORS

Topological resonator is a burgeoning platform integrating topological phases and cavity dynamics. Here we demonstrate a triangle topological resonator enforcing the DKS combs in a Si_3N_4 VPC slab. As depicted in Fig. 1(a), a scheme of the VPC topological resonator is designed to produce topological frequency combs, where a bus wave guide is used to couple the pump into the resonator. When a CW laser is pumped at a resonator frequency, the third-order nonlinearity of Si_3N_4 material with appropriate dispersion leads to a frequency comb with the spacing of free spectral range (FSR). When it meets a balance between intrinsic dispersion and nonlinearity-induced parametric gain, the comb shows a fully coherent formation, so-called DKSs. Since the DKS comb is produced in the triangle topological resonator, it is inborn topological. Such topological protection brings the DKS combs robustness against sharp corners.

The two-dimensional (2D) close-up image of VPCs is shown in Fig. 1(b), which is composed of VPC_1 and VPC_2 [29,30]. The nanohole sizes are determined by d_1 and d_2, where the lattice constant is $a = 300$ nm. As shown in Fig. 1(c), the calculated band structures of different VPCs reveal that there is a Dirac cone at the K and K′ valleys, as illustrated by green dots. The equilateral triangular nanoholes with C_6 lattice symmetry preserve a graphenelike lattice model [30]. This lattice symmetry leads to degenerate Dirac points at the K and K′ valleys in the Brillouin zone. With the distortion of the unit cell ($d_1 = 0.25a$, and $d_2 = 0.75a$), it opens a photonic bandgap at the Dirac cone due to the breaking of lattice symmetry, as displayed by red dots in

Fig. 1(c). Theoretically, the valley Chern numbers of VPC_1 and VPC_2 are described by $C_{K/K'} = \pm 1/2$, respectively [34]. Therefore, the difference between the valley Chern number of VPC_1 and VPC_2 is calculated as $|\Delta C_{K/K'}| = 1$. According to bulk-boundary correspondence, there exists one edge state in each valley. The two edge states are locked to K and K′ valleys, respectively, which refers to "valley-locked" chirality. This QVH model exhibits valley kink states propagating along the interface between VPC_1 and VPC_2, which shows robustness against certain disorders.

To study the underlying properties of topological VPCs, we perform the band calculation of VPCs. As shown in Fig. 2(a), the band opens a large gap from 361 THz to 380 THz. There exists a pair of valley-polarized topological kink states (corresponding to $k_x > 0$ and $k_x < 0$, respectively) in the complete bandgap. Therefore, there is only a single mode for a given wave vector k_x, which avoids the mode competition in FWM processes. The group velocity for the edge state within the band gap is nearly constant. Note that this pair of valley-polarized kink states exhibit opposite group velocity and opposite polarizations, referred to as left-handed circular polarization (LCP) and right-handed circular polarization (RCP), respectively. Also, valley kink states are robust against defects and sharp corners [34]. In addition, the light confinement of propagating modes along the interface results in the high-efficiency generation of frequency combs. For the resonators producing the optical frequency combs, the developed dispersion engineering, so-called integrated dispersion, plays an important role in comb formation [1]. A mode number μ is used to index the relative resonator mode counted concerning the pump mode ω_0, where the pump mode ω_0 is selected around the middle of all resonator modes to produce more signal and idler sidebands via FWM processes. The indexed resonance modes ω_μ can be Taylor expanded around the pumped mode ω_0:

$$\omega_\mu = \omega_0 + \mu D_1 + \frac{D_2}{2}\mu^2 + \frac{D_3}{6}\mu^3 = \omega_0 + \sum_i^\infty D_i \frac{\mu^i}{i!}, \quad (1)$$

where the expansion term is described as $D_i = d^i\omega_\mu/d\mu^i$ at $\omega = \omega_0$. The first-order term D_1 is related to the FSR of the resonator, which can be calculated as $D_1 = \Delta\omega_{FSR} = (\omega_1 - \omega_{-1})/2$. The second-order dispersion term D_2 corresponds to the group velocity dispersion (GVD): $D_2 = \omega_1 + \omega_{-1} - 2\omega_0$. Furthermore, it is convenient to define the integrated dispersion D_{int} as

$$D_{int}(\mu) = \omega_\mu - (\omega_0 + \mu D_1) = \frac{D_2}{2}\mu^2 + \frac{D_3}{6}\mu^3 + \cdots. \quad (2)$$

Integrated dispersion D_{int} contains high-order dispersion terms of the resonator and can be calculated from the transmission spectrum. Figure 2(b) shows dispersions of the topological resonator extracted from the simulated transmission [Fig. 2(c)], which indicates an anomalous GVD case with $D_2 > 0$. Anomalous GVD is crucial for the generation of parametric oscillations and Kerr solitons, which allows the optical frequency combs to span a bandwidth far exceeding the anomalous dispersion region [1,38].

Topological resonators based on VPCs have been proposed to conduct the lasing [39,40], optical routing [41],
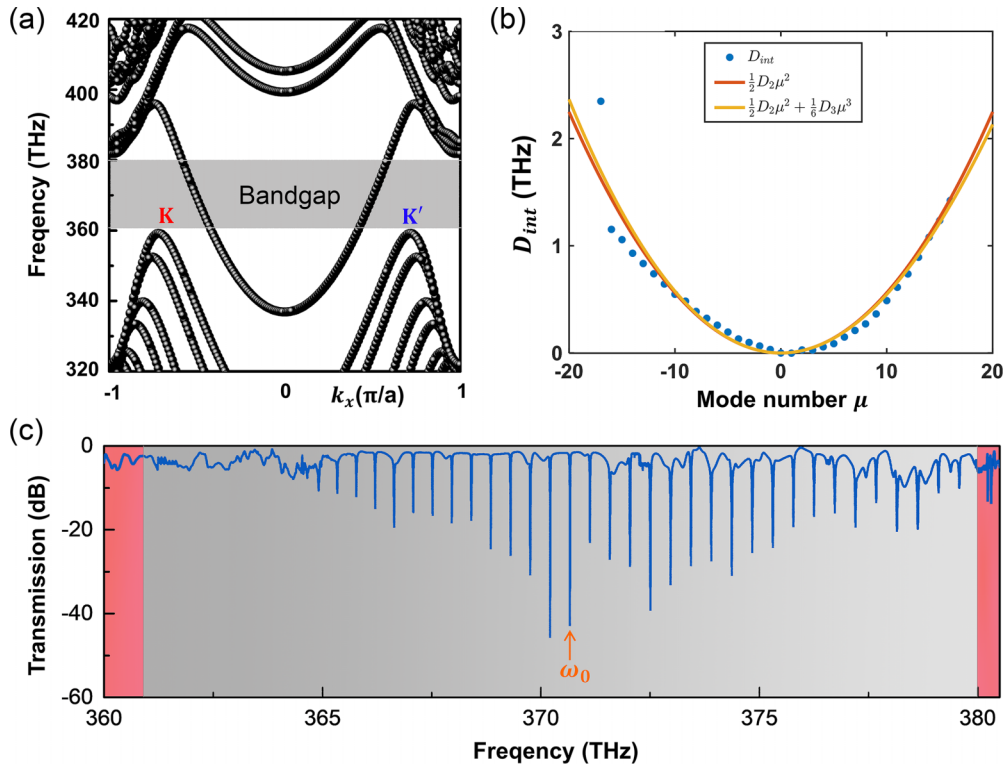
FIG. 2. (a) Calculated dispersion relation of valley kink states composed of VPC$_1$ and VPC$_2$. (b) Dispersions of the topological resonator. (c) Transmission spectrum of kink states for the topological resonator.

filters [42], and quantum emitter [43]. Here we proposed a triangle topological resonator to produce DKS combs. A straight topological bus wave guide is used to couple the pump mode into the topological resonator, and then guide the generated combs from the resonator to the bus wave guide. The gap width between the bus wave guide and the topological resonator is three cells. We numerically simulate the transmission spectrum of kink states for the topological resonator. As shown in Fig. 2(c), the resonator modes with identical frequency separation (so-called FSR) can be observed. Such identical frequency spacing indicates the modes circulating inside the triangular cavity, which can be recognized as whispering-gallery modes in topological resonators [39]. It is clear evidence that the topological resonator leads to an FSR of 450 GHz. A complete distinction is observed between topological bandgap and bulk states. For the region of bulk states, there is no resonator mode existing. Due to the excitations of valley kink states, topological optical frequency combs only appear at frequencies inside the topological bandgap.

The Lorentzian fitting of the simulated resonant dip at the pump frequency of 370.67 THz reveals a total Q factor of 8.86×10^4 [34]. The external loss κ_{ex} and intrinsic loss κ_{in} are calculated as $\kappa_{in} = \kappa_{ex} = 1.35 \times 10^{10}$ rad/s. Correspondingly, the intrinsic quality factor Q_{in} and external quality factor Q_{ex} are calculated as $Q_{in} = Q_{ex} = 1.772 \times 10^5$. Therefore, the coupling efficiency of the topological resonator satisfies $\eta = \kappa_{ex}/(\kappa_{ex} + \kappa_{in}) = 1/2$, leading to the critical coupling [1]. The threshold for parametric oscillation in the resonator is proportionable to V_0/Q^2, where V_0 is the effective

volume of the pump. Hence, generating signal and idler sidebands from FWM is easy to manipulate in such high-Q VPC resonators.

Thanks to the intrinsic nonlinearity of the resonator, numerous sidebands with equidistant gaps are produced in the resonator with the injection of a CW pump laser at the angular frequency of ω_0 (indexed by the number $\mu = 0$). To visualize the stimulated FWM process of the topological resonator, we simulate the electric field profiles of the FWM process with the selected signal and idler frequencies ($\mu = 1, -1$). Such numerical model of the FWM process in VPCs is performed in the software COMSOL Multiphysics [34]. As depicted in Fig. 3, the kink states of the pump, signal, and idler are excited in the coupled wave guide-resonator device. A circularly polarized excitation is used to emulate kink states along the bus wave guide. Since the pump frequency is consistent with the resonator mode ω_0, the injected pump is coupled to the topological resonator and excites the FWM process simultaneously. This chirality is also preserved for the cavity due to the same topology between the bus wave guide and the triangle cavity. There is no input for the kink state of the idler, thus, the generation of field profiles at the idler frequency gives clear evidence of the FWM processes [25]. The field profiles of topological resonator modes are concentrated at the interface, resulting in the high-efficiency generation of the FWM process. Remarkably, the resonator modes show robustness against sharp bends, confirming the topological nature of the QVH effect. Note that the direction of rotation in the topological ring is related to the injected pump mode [34].
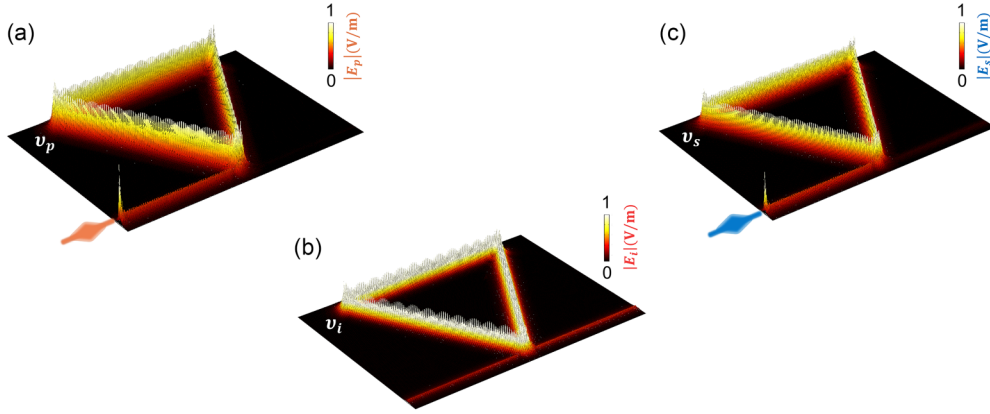
FIG. 3. Field profiles of the stimulated FWM process in the topological resonator at frequencies of the (a) pump ($v_p = 370.67$ THz), (b) idler ($v_i = 370.21$ THz), and (c) signal ($v_s = 371.13$ THz) respectively.

III. TOPOLOGICAL KERR SOLITON COMBS

DKS combs can be readily implemented in topological microresonators due to the intrinsic Kerr nonlinearity of nonlinear materials [17]. DKSs are temporal solutions to the balance between intrinsic dissipation and nonlinearity-induced parametric gain [1]. When the parametric gain of the cavity exceeds the decay rate, symmetrically spaced sidebands appear around the incident pump. Optical frequency combs can grow to DKSs with the tuning of the frequency of the pump laser. Unlike the complex arrays of coupled rings emulating the SSH model, in our triangular photonic crystal cavity, we can only consider the coupling between a topological wave guide and a cavity. Thanks to the topological protection of valley kink states, light can transport smoothly along sharp bends with negligible scattering and reflection. Our topological resonator is analogous to a traditional whispering-gallery cavity, where light traveling inside the whispering-gallery cavity is equivalently considered as traveling along a straight wave guide with boundary conditions of the resonators. Therefore, the nonlinear dynamics of light inside our topological resonator can be briefly simulated by a single-ring Lugiato-Lefever equation (LLE). In general, the dynamics of optical frequency combs in the microresonator are described by LLE [37,44]:

$$\frac{\partial}{\partial \tau} A = -\left(\frac{\kappa}{2} + i\delta\omega\right)A + i\pi \cdot FSR \cdot D_2 \frac{\partial^2}{\partial T^2}A$$
$$+ iL \cdot FSR \cdot \gamma |A|^2 A + \sqrt{\frac{\kappa \eta P_{in}}{\hbar \omega}}, \quad (3)$$

where A describes the evolution of the intracavity field, κ is related to the linewidth of resonator modes, and $\delta\omega$ is the detuning of the resonance frequency. With proper approximations of the LLE, the dynamics of DKSs can be numerically simulated [34]. To access the reproducible soliton state, the pump is detuned from the blue ($\delta\omega < 0$) to the red region ($\delta\omega > 0$). In general, the evolution of optical frequency combs is recognized by several trajectories, including Turing rolls, chaotic states, breathing solitons, and eventually into the soliton states [1]. In the case of single soliton states, the comb

spectrum is almost smooth and phase locked [45]. Such single soliton states have been experimentally observed in a great deal of platforms [5,8–10], therefore, we can conclude several tricks to excite single soliton states. First, solitons are always generated at the red tuning of resonance frequency where the intracavity field is bistable [1]. Second, the combs of single soliton formation take parallel shapes of sech^2 functions. Third, in the time domain, multiple or single soliton states behave with several spaced pulses or one ultrashort pulse upon a period of the round-trip time.

To numerically simulate the dynamic evolution of the topological resonator, we consider a whisper-gallery topological resonator. The input pump frequency ω_0 corresponds to the resonance frequency indexed by $\mu = 0$, leading to the generation of the spaced sidebands in other resonator modes ($\mu \neq 0$) via FWM processes. Since the pattern of the topological resonator is constructed by interfaces between VPC$_1$ and VPC$_2$, the optical frequency combs are generated at the interfaces, and they transport along a certain triangular path. However, when the incident pump is coincident with bulk bands, the output comb is barely visible. In the case of bulk modes, the incident pump is dissipated into the photonic crystals. Due to the topological protection of valley kink states, the backscattering around the sharp corners is negligible [46]. Therefore, the reflection of resonator modes at the sharp corners is not included in our theoretical model.

In our simulation, the actual pump power is 2.2 W, and the refractive index of Si$_3$N$_4$ is 2.0, with the nonlinear index 2.5×10^{-19} m^{2}W^{-1}. The FSR and dispersion D_2 are extracted from the simulated transmission [Fig. 2(c)], with calculated values of $FSR = 450$ GHz and $D_2 = 9.53$ GHz. We note that the simulations of soliton existences are related to dispersion D_2, therefore, the certain lattice defects that lead to the breaking of dispersion shape could destroy the presence of solitons. The simulated total Q factor indicates a value of 8.86×10^4. The external loss and the total energy loss rate of the resonator are calculated as $\kappa_{ex} = 1.35 \times 10^{10}$ rad/s and $\kappa = 2.7 \times 10^{10}$ rad/s. In this case, the coupling efficiency of critical coupling is given by $\eta = 1/2$. The length of the topological resonator is $L = 3l$, where $l = 180a$ is the side length of
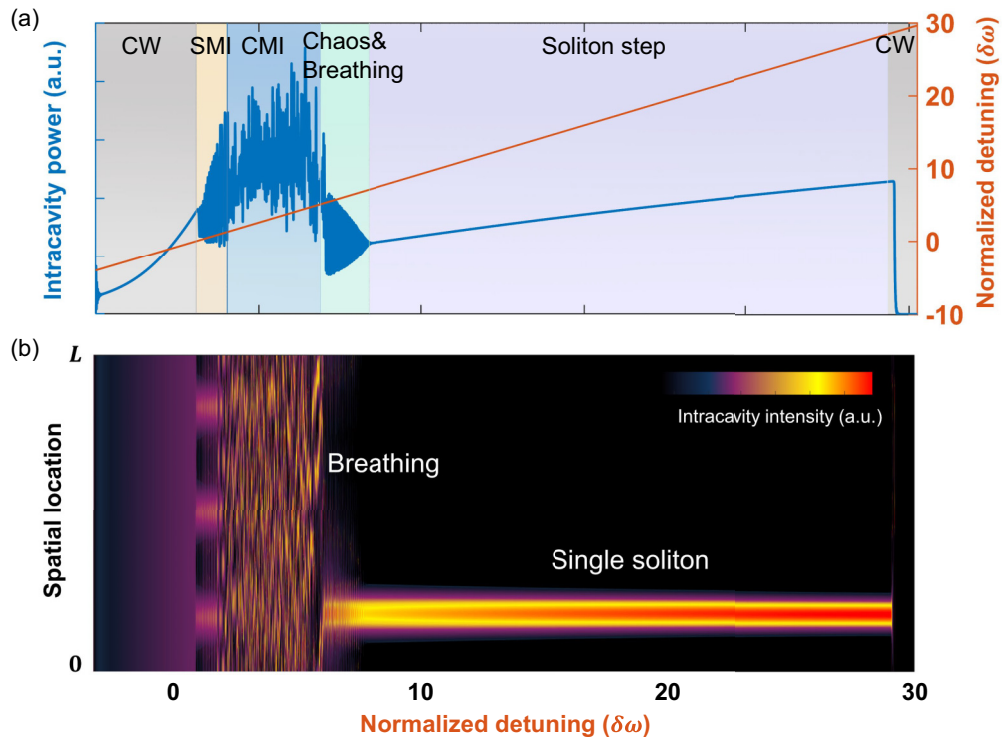
FIG. 4. Numerical simulated evolution of soliton formation in a topological resonator. (a) Effective intracavity energy evolution with the detuning from blue-detuned to red-detuned region. There appear three conspicuous processes including Turing rolls, chaotic states (breathing solitons), and single soliton states, respectively. (b) Corresponding spatiotemporal evolution of soliton formation.

the triangular configuration. We assume the effective field cross-section area $A_{\text{eff}} = 2.1 \times 10^{-14} \text{m}^2$, and the nonlinear coefficient of the topological resonator is given by $\gamma = \omega_0 n_2 / c A_{\text{eff}}$. We believe our topological DKSs can be experimentally accessed by present nanofabrication technology [45,47].

The simulated dynamic evolution of topological DKSs as a function of detuning is illustrated in Fig. 4(a). The corresponding spatiotemporal evolution of the DKS excitation process is shown in Fig. 4(b). Three conspicuous forms are identified during the evolution process, that is, Turing rolls, chaotic states (breathing solitons), and single soliton states, respectively. Figure 5 shows the spatial intensity distribution of the generated pulses with different detuning of the pump in the topological resonator, which can also be accessed from the spatiotemporal evolution [34]. The pulses are circulated along the edge of the triangle topological resonator in a clockwise direction as time evolves.

In the early stages of evolution, the intensity build-up process leads to the increasing of intracavity power with the detuning from the blue side. The temporal pattern shows three equally spaced pulses within the triangular resonator, which is referred to as Turing rolls. Those stable pulses are attributed to the self-stabilization of the nonlinear evolution in the blue-detuned side of the resonance frequency. Thus, such a stage of modulation instability is referred to as stable modulation instability (SMI). We can observe that the cavity energy varies smoothly in the case of Turing rolls.

Those chaotic states are followed by the nonstationary behavior-breathing soliton states. Figure 5(c) shows that there is only one pulse inside the topological resonator with the detuning $\delta\omega = 6.13$; the amplitude and duration of the intracavity waveform are oscillated periodically, where the oscillation period is regarded as the breathing period. Correspondingly, the combs show periodical compression and stretching. Such instability occurs at the furcation of chaos and a stable DKS, which is referred to as Hopf bifurcation.

When the pump is further detuned to the red side ($\delta\omega = 28.73$), actual soliton formation can be accessed because the intracavity field is bistable. The intracavity power shows the formation of a "step" characteristic; this "step" is the identification of solitons. The "length" of the soliton step corresponds to the pump power. For the intracavity energy, the oscillation quickly evolves to a relatively stable situation. This bistable state is an elaborate consequence of the off-resonance pump detuning $\delta\omega$ and Kerr nonlinear shift of the resonator.

As shown in Fig. 4(b), the corresponding spatiotemporal formation of single soliton states also exhibits intriguing results. A quick comparison with the spatiotemporal intensity distribution of Turing rolls and chaotic states reveals that there exists only one ultrashort pulse upon a period of the round-trip time for a single soliton state. Once a single soliton state is accessed, the thermal nonlinearity of solitons makes the laser-cavity detuning self-stabilized. In this scenario, single soliton states can be stable for several hours. Note that multiple solitons may exist in the cavity where the number of emerging solitons is random [1]. Proceeding further, the comb
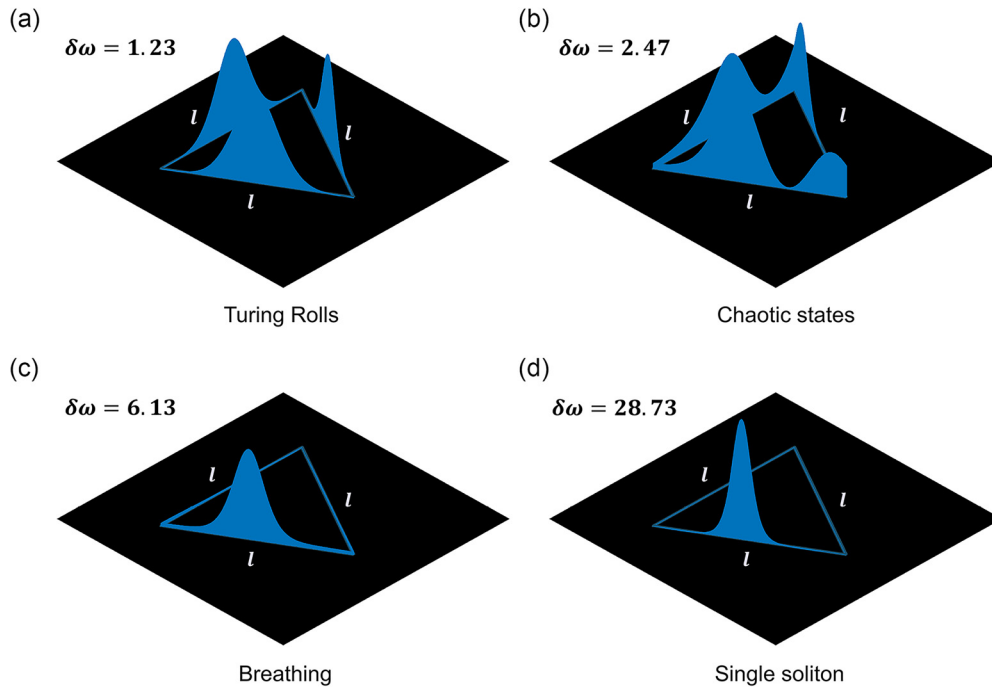
FIG. 5. Spatial intensity distribution of the (a) Turing rolls, (b) chaotic states, (c) breathing, and (d) single soliton state, respectively.

degenerates to a continuous component due to the separation of the pump and resonance frequency.

The formations of corresponding optical frequency combs are shown in Fig. 6. It is noted that generated Kerr frequency combs are composed of a CW pump component and relatively weak bilateral combs [6]. When the nonlinear gain overcomes the cavity losses, the developed primary comb so-called Turing rolls is generated. As seen in Fig. 6(a), the comb amplitudes of Turing rolls have distinct contrast.

When the pump is further detuned to the red side, the increasing intracavity power initiates FWM processes, which leads to secondary sidebands and subcombs. The output comb of chaotic states is depicted in Fig. 6(b), Random variations of combs indicate that there is no stationary solution existing, leading to the incoherence of the wave form.

Following chaotic states, the generation of breathing solitons means the arrival of a low-detuning boundary of the soliton. As depicted in Fig. 6(c), the comb of breathing soli-
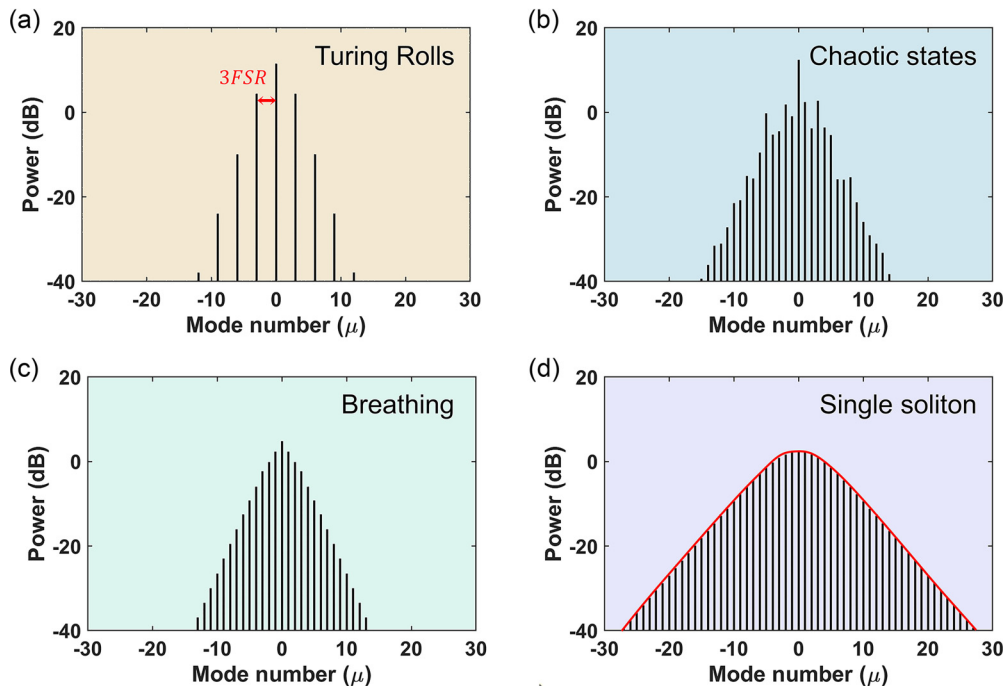

FIG. 6. Simulated optical frequency combs of (a) Turing rolls, (b) chaotic states, (c) breathing solitons, and (d) single soliton states.

tons takes the form of a triangular feature. Note that the amplitudes of the comb oscillate with the breathing period, and the comb returns to its initial state after one period.

The self-sustaining wave packets of the single soliton state indicate that comb lines are phase locked with each other [Fig. 6(d)]. More importantly, the shape of the spectral output takes the form of $sech^2$ functions. This behavior of a single soliton state in the topological resonator is analogous to that observed in Si_3N_4 single-ring resonators where single solitons exist [1]. Note that if the pump and dissipation are ideally turned off, the propagating time of soliton in our topological resonator is related to photon lifetime, which can be calculated by $\tau_p = Q/\omega_0 = 38.04$ ps.

We have shown many resemblances between topological resonators and single-ring resonators, however, for the DKS and single soliton combs produced in our design, thanks to the topological nature of VPCs, they are inherited to be robust against sharp bends and certain disorders. In the experimental realization, the strong thermal effect becomes an intractable element to produce stable solitons in the red-detuned region. To overcome this, heaters can be used to control the temperature of VPC chips [45,47]. Based on the state-of-the-art nanofabrication technology, our topological DKS combs design could be implemented experimentally.

IV. CONCLUSION

In this work, we have demonstrated a theoretical scheme exhibiting topological optical frequency combs and DKS combs. The triangle resonator is composed of VPCs with different topologies and can excite topological valley kink resonator modes propagating along the interface. We numerically simulate the nonlinear dynamic evolution of the topological resonator with the injection of the pump laser. The result reveals that the single soliton states can be produced in the resonator, and they are born to be topological. This topological nature endows the DKS combs' robustness against sharp bends and disorders. Our topological frequency combs could be readily accessed in on-chip nanofabricated photonics.

[1] T. J. Kippenberg, A. L. Gaeta, M. Lipson, and M. L. Gorodetsky, Dissipative kerr solitons in optical microresonators, Science **361**, eaan8083 (2018).

[2] Q.-F. Yang, X. Yi, K. Y. Yang, and K. Vahala, Stokes solitons in optical microcavities, Nat. Phys. **13**, 53 (2017).

[3] C. Bao, J. A. Jaramillo-Villegas, Y. Xuan, D. E. Leaird, M. Qi, and A. M. Weiner, Observation of fermi-pasta-ulam recurrence induced by breather solitons in an optical microresonator, Phys. Rev. Lett. **117**, 163901 (2016).

[4] D. C. Cole, E. S. Lamb, P. Del'Haye, S. A. Diddams, and S. B. Papp, Soliton crystals in kerr resonators, Nat. Photonics **11**, 671 (2017).

[5] W. Liang, D. Eliyahu, V. S. Ilchenko, A. A. Savchenkov, A. B. Matsko, D. Seidel, and L. Maleki, High spectral purity kerr frequency comb radio frequency photonic oscillator, Nat. Commun. **6**, 7957 (2015).

[6] T. Herr, V. Brasch, J. D. Jost, C. Y. Wang, N. M. Kondratiev, M. L. Gorodetsky, and T. J. Kippenberg, Temporal solitons in optical microresonators, Nat. Photonics **8**, 145 (2014).

[7] X. Yi, Q.-F. Yang, K. Y. Yang, M.-G. Suh, and K. Vahala, Soliton frequency comb at microwave rates in a high-q silica microresonator, Optica **2**, 1078 (2015).

[8] V. Brasch, M. Geiselmann, T. Herr, G. Lihachev, M. H. Pfeiffer, M. L. Gorodetsky, and T. J. Kippenberg, Photonic chip–based optical frequency comb using soliton cherenkov radiation, Science **351**, 357 (2016).

[9] L. Zhou, Y. Shen, C. Xi, X. Huang, and G. He, Computer-controlled microresonator soliton comb system automating soliton generation and expanding excursion bandwidth, Optics Continuum **1**, 161 (2022).

[10] C. Joshi, J. K. Jang, K. Luke, X. Ji, S. A. Miller, A. Klenner, Y. Okawachi, M. Lipson, and A. L. Gaeta, Thermally controlled comb generation and soliton modelocking in microresonators, Opt. Lett. **41**, 2565 (2016).

[11] Y. He, Q.-F. Yang, J. Ling, R. Luo, H. Liang, M. Li, B. Shen, H. Wang, K. Vahala, and Q. Lin, Self-starting bi-chromatic linbo 3 soliton microcomb, Optica **6**, 1138 (2019).

[12] Z. Gong, X. Liu, Y. Xu, M. Xu, J. B. Surya, J. Lu, A. Bruch, C. Zou, and H. X. Tang, Soliton microcomb generation at 2 μm in z-cut lithium niobate microring resonators, Opt. Lett. **44**, 3182 (2019).

[13] M. Pu, L. Ottaviano, E. Semenova, and K. Yvind, Efficient frequency comb generation in algaas-on-insulator, Optica **3**, 823 (2016).

[14] D. Smirnova, S. Kruk, D. Leykam, E. Melik-Gaykazyan, D.-Y. Choi, and Y. Kivshar, Third-harmonic generation in photonic topological metasurfaces, Phys. Rev. Lett. **123**, 103901 (2019).

[15] S. S. Kruk, W. Gao, D.-Y. Choi, T. Zentgraf, S. Zhang, and Y. Kivshar, Nonlinear imaging of nanoscale topological corner states, Nano Lett. **21**, 4592 (2021).

[16] J. W. You, Z. Lan, and N. C. Panoiu, Four-wave mixing of topological edge plasmons in graphene metasurfaces, Sci. Adv. **6**, eaaz3910 (2020).

[17] S. Mittal, G. Moille, K. Srinivasan, Y. K. Chembo, and M. Hafezi, Topological frequency combs and nested temporal solitons, Nat. Phys. **17**, 1169 (2021).

[18] Z. Jiang, H. Wang, Y. Yang, Y. Shen, B. Ji, Y. Chen, Y. Zhang, L. Sun, Z. Wang, C. Jiang *et al.*, On-chip topological transport of optical frequency combs in silicon-based valley photonic crystals, arXiv:2310.15629.

[19] Y. V. Kartashov and D. V. Skryabin, Bistable topological insulator with exciton-polaritons, Phys. Rev. Lett. **119**, 253904 (2017).

[20] R. Banerjee, S. Mandal, and T. C. H. Liew, Coupling between exciton-polariton corner modes through edge states, Phys. Rev. Lett. **124**, 063901 (2020).

[21] D. A. Smirnova, L. A. Smirnov, D. Leykam, and Y. S. Kivshar, Topological edge states and gap solitons in the

nonlinear dirac model, Laser Photonics Rev. **13**, 1900223 (2019).

[22] N. Pernet, P. St-Jean, D. D. Solnyshkov, G. Malpuech, N. Carlon Zambon, Q. Fontaine, B. Real, O. Jamadi, A. Lemaitre, M. Morassi *et al.*, Gap solitons in a one-dimensional driven-dissipative topological lattice, Nat. Phys. **18**, 678 (2022).

[23] S. Mittal, E. A. Goldschmidt, and M. Hafezi, A topological source of quantum light, Nature (London) **561**, 502 (2018).

[24] Y. Chen, X.-T. He, Y.-J. Cheng, H.-Y. Qiu, L.-T. Feng, M. Zhang, D.-X. Dai, G.-C. Guo, J.-W. Dong, and X.-F. Ren, Topologically protected valley-dependent quantum photonic circuits, Phys. Rev. Lett. **126**, 230503 (2021).

[25] Z. Jiang, Y. Ding, C. Xi, G. He, and C. Jiang, Topological protection of continuous frequency entangled biphoton states, Nanophotonics **10**, 4019 (2021).

[26] Z. Jiang, C. Xi, G. He, and C. Jiang, Topologically protected energy-time entangled biphoton states in photonic crystals, J. Phys. D **55**, 315104 (2022).

[27] S. Mittal, V. V. Orre, E. A. Goldschmidt, and M. Hafezi, Tunable quantum interference using a topological source of indistinguishable photon pairs, Nat. Photonics **15**, 542 (2021).

[28] F. Gao, H. Xue, Z. Yang, K. Lai, Y. Yu, X. Lin, Y. Chong, G. Shvets, and B. Zhang, Topologically protected refraction of robust kink states in valley photonic crystals, Nat. Phys. **14**, 140 (2018).

[29] Y. Yang, Y. Yamagami, X. Yu, P. Pitchappa, J. Webber, B. Zhang, M. Fujita, T. Nagatsuma, and R. Singh, Terahertz topological photonics for on-chip communication, Nat. Photonics **14**, 446 (2020).

[30] M. I. Shalaev, W. Walasik, A. Tsukernik, Y. Xu, and N. M. Litchinitser, Robust topologically protected transport in photonic crystals at telecommunication wavelengths, Nat. Nanotechnol. **14**, 31 (2019).

[31] H. Wang, L. Sun, Y. He, G. Tang, S. An, Z. Wang, Y. Du, Y. Zhang, L. Yuan, X. He *et al.*, Asymmetric topological valley edge states on silicon-on-insulator platform, Laser Photonics Rev. **16**, 2100631 (2022).

[32] X.-T. He, E.-T. Liang, J.-J. Yuan, H.-Y. Qiu, X.-D. Chen, F.-L. Zhao, and J.-W. Dong, A silicon-on-insulator slab for topological valley transport, Nat. Commun. **10**, 872 (2019).

[33] A. Tusnin, A. Tikan, K. Komagata, and T. J. Kippenberg, Dissipative structures in topological lattices of nonlinear optical resonators, Commun. Phys. **6**, 317 (2023).

[34] See Supplemental Material at http://link.aps.org/supplemental/10.1103/PhysRevB.108.205421 for (i) numerical simulation, (ii) valley topological photonics (vpcs), (iii) topological edge states, (iv) dispersion engineering, (v) coupling between wave guide and topological resonators, (vi) topological resonator modes, and (vi) numerical simulation of DKS combs in topological resonators, which also includes Refs. [35–37].

[35] J. Lu, C. Qiu, L. Ye, X. Fan, M. Ke, F. Zhang, and Z. Liu, Observation of topological valley transport of sound in sonic crystals, Nat. Phys. **13**, 369 (2017).

[36] J. Noh, S. Huang, K. P. Chen, and M. C. Rechtsman, Observation of photonic topological valley Hall edge states, Phys. Rev. Lett. **120**, 063902 (2018).

[37] L. A. Lugiato and R. Lefever, Spatial dissipative structures in passive optical systems, Phys. Rev. Lett. **58**, 2209 (1987).

[38] Y. Okawachi, M. R. Lamont, K. Luke, D. O. Carvalho, M. Yu, M. Lipson, and A. L. Gaeta, Bandwidth shaping of microresonator-based frequency combs via dispersion engineering, Opt. Lett. **39**, 3535 (2014).

[39] Y. Zeng, U. Chattopadhyay, B. Zhu, B. Qiang, J. Li, Y. Jin, L. Li, A. G. Davies, E. H. Linfield, B. Zhang *et al.*, Electrically pumped topological laser with valley edge modes, Nature (London) **578**, 246 (2020).

[40] H. Zhong, Y. Li, D. Song, Y. V. Kartashov, Y. Zhang, Y. Zhang, and Z. Chen, Topological valley hall edge state lasing, Laser Photonics Rev. **14**, 2000001 (2020).

[41] J. Ma, X. Xi, and X. Sun, Topological photonic integrated circuits based on valley kink states, Laser Photonics Rev. **13**, 1900087 (2019).

[42] L. Gu, Q. Yuan, Q. Zhao, Y. Ji, Z. Liu, L. Fang, X. Gan, and J. Zhao, A topological photonic ring-resonator for on-chip channel filters, J. Lightwave Technol. **39**, 5069 (2021).

[43] S. Barik, A. Karasahin, S. Mittal, E. Waks, and M. Hafezi, Chiral quantum optics using a topological resonator, Phys. Rev. B **101**, 205303 (2020).

[44] Y. K. Chembo and C. R. Menyuk, Spatiotemporal lugiato-lefever formalism for kerr-comb generation in whispering-gallery-mode resonators, Phys. Rev. A **87**, 053852 (2013).

[45] A. L. Gaeta, M. Lipson, and T. J. Kippenberg, Photonic-chip-based frequency combs, Nat. Photonics **13**, 158 (2019).

[46] H. Wang, G. Tang, Y. He, Z. Wang, X. Li, L. Sun, Y. Zhang, L. Yuan, J. Dong, and Y. Su, Ultracompact topological photonic switch based on valley-vortex-enhanced high-efficiency phase shift, Light Sci. Appl. **11**, 292 (2022).

[47] W. Wang, L. Wang, and W. Zhang, Advances in soliton microcomb generation, Adv. Photonics **2**, 034001 (2020).